JGR Oceans

RESEARCH ARTICLE
10.1029/2024JC021399

Key Points:
- Surface drifters were used to measure turbulence within strong diurnal warm layers (DWL) in the Southern California Bight
- Turbulent kinetic energy (TKE) dissipation rates ϵ exhibit strong modulation by the DWL, and simple models underestimate observed values
- Bulk Richardson numbers suggest DWL are unstable, and periodic structures on the layer scale are observed when ϵ values are high

Correspondence to:
K. Zeiden,
kzeiden@uw.edu

Citation:
Zeiden, K., Thomson, J., Shcherbina, A., & D'Asaro, E. (2024). Observations of elevated mixing and periodic structures within diurnal warm layers. *Journal of Geophysical Research: Oceans*, *129*, e2024JC021399. https://doi.org/10.1029/2024JC021399

Received 29 MAY 2024
Accepted 18 OCT 2024

Author Contributions:
Conceptualization: Kristin Zeiden, Jim Thomson, Andrey Shcherbina, Eric D'Asaro
Data curation: Kristin Zeiden
Formal analysis: Kristin Zeiden
Funding acquisition: Jim Thomson
Methodology: Kristin Zeiden, Eric D'Asaro
Project administration: Jim Thomson
Supervision: Jim Thomson
Writing – original draft: Kristin Zeiden
Writing – review & editing: Kristin Zeiden, Jim Thomson, Andrey Shcherbina, Eric D'Asaro

Observations of Elevated Mixing and Periodic Structures Within Diurnal Warm Layers

Kristin Zeiden[1], **Jim Thomson**[1], **Andrey Shcherbina**[1], **and Eric D'Asaro**[1]

[1]Applied Physics Laboratory, University of Washington, Seattle, WA, USA

Abstract Surface drifters (SWIFTs) equipped with down-looking high-resolution acoustic doppler current profilers (ADCPs) were used to estimate the turbulent kinetic energy (TKE) dissipation rate (ϵ) within highly stratified diurnal warm layers (DWLs) in the Southern California Bight. Over a 10-day period, five instances of DWLs were observed with strong surface temperature anomalies up to 3°C and velocity anomalies up to 0.3 m s^{-1}. Profiles of ϵ in the upper 5 m suggest turbulence is strongly modulated by the DWL stratification. Burst-averaged (8.5 min) ϵ is stronger than predicted by law-of-the-wall boundary layer scaling within the DWLs and suppressed below. Predictions for ϵ within the DWLs are improved by a shear-production scaling using observed shear and linearly decaying turbulent stress. However, ϵ is still under-predicted. Examination of the un-averaged acoustic backscatter data suggests elevated ϵ is related to the presence of turbulent structures in the DWLs which span the layer height and strongly modulate TKE. Evolution in the bulk Richardson number each day suggests the DWLs become unstable to layer-scale overturning and entrainment each afternoon, thus the turbulent structures may result from shear-driven instability. This interpretation is supported by a conditional average of the data during a burst characterized by strongly periodic structures. The structures resemble high-frequency internal waves with strong asymmetry in the along-flow direction (steepening) which suggests they are unstable. Coincident asymmetric patterns in upwelling/downwelling and corresponding regions of strong vertical convergence/divergence suggest that both vertical transport and local TKE generation are plausible sources of elevated ϵ in the DWLs.

Plain Language Summary Diurnal warm layers (DWLs) are thin surface layers of very warm water which have significant impact on how heat and momentum are exchanged between the ocean and atmosphere. In this study, a fleet of autonomous floats were deployed in the open ocean to measure turbulence within a few meters of the ocean surface. During the experiment, the floats observed strong turbulence within shallow (1–10 m) warm layers created by daily heating of the ocean surface. These warm layers were particularly strong, up to 3 °C warmer than the ocean below, and strongly modulated turbulence magnitudes. Simple models used to predict the rate of turbulent kinetic energy (TKE) dissipated to heat were found to under-predict the observed values. A dynamic analysis suggests that the layers are likely unstable to turbulent overturning, due to strong vertical gradients in velocity. Consistent with this analysis, close examination of the high-resolution turbulence data revealed the presence of periodic structures which spanned the height of the layers. The structures had strong vertical velocities and significantly modulated TKE, suggesting they may be the source of elevated dissipation rates.

1. Introduction

Diurnal warm layers (DWLs) are thin (1–10 m) anomalously warm (up to a few °C) layers at the ocean surface generated by solar heating. Warming creates stable near-surface stratification, which acts against the downward transfer of momentum from the wind to the ocean, suppressing turbulence. A surface current anomaly can develop in response, along with corresponding strong shear (e.g., Shcherbina et al., 2019). DWL shear is hypothesized to become unstable and transfer energy from the mean flow to turbulence, which erodes the stratification and deepens the DWL over the course of the day (Price et al., 1986). This cycle of turbulence suppression and enhancement by DWLs modulates gas and heat fluxes from the atmosphere to the rest of the mixed layer. Thus predicting the evolution of turbulence is key to accurately modeling ocean surface boundary layer (OSBL) dynamics. However, observations of turbulence in DWLs are rare. This is in part due to the difficulty in sampling at sufficiently high spatial and temporal resolution near the ocean surface. There are significant measurement challenges inherent in making observations relative to the moving air-sea interface, as well as distinguishing between surface gravity wave shear and turbulence. In this study, we present observations of turbulent vertical velocity and turbulent kinetic energy dissipation rate (ϵ) within DWLs obtained with surface wave instrument floats with tracking (SWIFTs).

1.1. Turbulence in DWLs

We are interested in understanding how turbulence is modulated by the presence of DWLs; however, turbulent vector velocities are extremely difficult to measure outside of the laboratory. An approachable proxy for turbulence in the ocean is turbulent kinetic energy dissipation rate, ϵ. Prior observations have revealed significant vertical modulation of near-surface ϵ by DWLs. Vagle et al. (2012) and later Moulin et al. (2018) describe a cycle where turbulence, inferred from measurements of ϵ, is initially suppressed below the very thin stably stratified DWL created in the first few hours of solar heating. Around midday, turbulence intensity within the layer increases and the layer begins to deepen. This strong turbulence is hypothesized to be driven by shear associated with the wind-driven surface current trapped within the layer (Price et al., 1986). At night, surface cooling drives convection which mixes away any remaining stratification. Near-surface turbulence remains elevated until the stratification is eroded.

Modulation of ϵ by the DWL is typically quantified by comparison with the law-of-the-wall scaling prediction for near-surface dissipation rate. There is observational support for law-of-the-wall in well-mixed (i.e., unstratified) surface layers in relatively calm conditions (i.e., limited wave forcing) and in bottom boundary layers (Kawaguchi et al., 2022; Perlin et al., 2005; Richman et al., 1987). Thus law-of-the-wall is often used as a baseline prediction for ϵ which is modulated by the presence of DWLs. Law-of-the-wall scaling arises from two primary assumptions: (a) turbulent shear stress is constant throughout the near-surface layer, which gives rise to a logarithmic velocity profile and corresponding shear given by the following equation:

$$S_*(z) = -u_*/\kappa z \tag{1}$$

and (b) shear production is balanced by turbulent dissipation such that

$$\epsilon_\tau(z) = u_*^2 S_*(z) \tag{2}$$

Here, u_* is the friction velocity of the water assumed to be set by wind stress τ, that is, $u_* = \sqrt{\tau/\rho}$, κ is the von Kármán constant equal to 0.41, z is distance from the surface ($z < 0$), and ρ is the water density. Together, Equations 1 and 2 imply

$$\epsilon_\tau(z) = -\frac{u_*^3}{\kappa z}. \tag{3}$$

Studies by Sutherland et al. (2016) and K. G. Hughes et al. (2020) found near-surface ϵ to be elevated relative to ϵ_τ within DWLs, and suppressed below. The sub-layer suppression of ϵ in particular supports the inference that momentum from the wind is confined by DWL stratification, but the magnitude of elevated ϵ within the layer is poorly constrained. Sutherland et al. (2016) attempted to improve the prediction by substituting the observed DWL shear ($S(z)$) for the law-of-the-wall shear prediction in Equation 2 ($S_*(z)$). They concluded that the observed shear was a better predictor of observed dissipation rates, but on average over-predicted observed values. However, that modification does not allow for any corresponding variation from the constant turbulent stress assumed in the law-of-the-wall model. Here, we similarly compare the observed ϵ to a modified version of Equation 2 in which the observed shear is substituted for the assumed logarithmic profile. As we do not know the true stress profile, we modify the model further by assuming linear decay from the surface as in the classic slab model:

$$\epsilon_S(z) = u_*^2(1 - z/H)S(z), \tag{4}$$

where H is the diurnal warm layer height. This formulation follows Zippel et al. (2022), who found a linear decay stress profile was sufficient to close the near-surface energy budget from observations of the wind stress and near-surface dissipation in the surface mixed layer within a factor of 2. We note two consequences of Equation 4 are (a) there is no shear within the mixed surface layer and (b) stress goes to zero below the layer. Implicit in our comparison is the assumption that deviations from this model in the true shear and stress profile are small.

1.2. Shear Instability

The source of elevated ϵ within DWLs during the day when stratification is stabilizing is hypothesized to be turbulent mixing driven by shear instability. Previous studies have shown that DWLs are intermittently characterized by small gradient Richardson numbers within the layer, $\mathrm{Ri} = N^2/S^2$, interpreted to be a condition for instability (e.g., K. Hughes et al., 2021). Here N is the buoyancy frequency and S is vertical shear. Ri weighs stabilizing buoyancy forcing against destabilizing inertial forcing at specific points in the flow (i.e., at fine scales). Flows with below-critical Ri are thought to be unstable and likely to overturn if sufficiently perturbed. Because coincident measurements of fine-scale stratification and shear are difficult to obtain, studies often use a “bulk” Richardson number across a stratified layer to gauge its stability,

$$Ri_b = \frac{g\Delta\rho H}{\rho_0(\Delta U)^2}. \tag{5}$$

Here $\Delta\rho$ and ΔU are representative velocity and density differences across the DWL, and H is the layer thickness. The physical consequence of below-critical Ri_b is less well established than Ri, but the literature suggests that overturning and entrainment occurs on the scale of the layer (Price et al., 1986). Further, while a critical value of 0.25 for Ri has been well established by numerical and laboratory studies, universal agreement on a critical value of Ri_b remains elusive. In their classic model of DWL evolution, Price et al. (1986) assign a value of 0.65. This is an empirical value which was initially determined by Price et al. (1978) using field observations of mixed layer deepening. The 0.65 threshold has subsequently been used in most 1-D bulk models (e.g., Fairall et al., 1996) to good effect. However, we emphasize that it has no dynamic basis.

Below-critical Ri is a necessary but not sufficient condition for shear-driven mixing. The strongest observational evidence of shear instability has been temperature “ramps” in DWLs, which have long been attributed to the passage of coherent stratified eddies past an array assumed to be Kelvin-Helmholtz billows (Thorpe, 1978). Similar observations by Moulin et al. (2018) and K. Hughes et al. (2021) show temperature ramps within descending DWLs concurrent with elevated ϵ and below-critical Ri. K. Hughes et al. (2021) bolstered these observations with a 2D model of DWL turbulence under similar forcing conditions, which showed the onset of shear-driven instability. In both studies ramps were coherent across the DWL suggesting turbulent structures, or at least their immediate precursors, with scales on par with the layer height. Beyond ramps in temperature time series and low Ri, observations which relate elevated DWL TKE or ϵ to the specific mechanism of shear instability are limited.

1.3. Study Overview

The primary observations in this study are profiles of dissipation rate and shear obtained from surface-following SWIFT drifters (Thomson, 2012). Temperature and density data were obtained with nearby profiling mixed layer floats (MLFs, D’Asaro et al., 1996). The data add to a small but growing body of literature showing strong modulation of turbulent dissipation rates and shear by DWL stratification. Estimates of Ri_b suggest that the layers are likely to overturn on the layer scale each afternoon and entrain cooler water from below. Consistent with this result, high-resolution “images” of acoustic backscatter reveal the presence of periodic structures which span the height of the layers. A novel result of this study is an illustrative case where structures were strongly periodic, enabling a conditional average of the structures (i.e., as a function of phase).

The paper is organized as follows: Section 2 describes the field experiment, instruments used and data collected. Section 3 describes the methods used to compute surface fluxes and dissipation rate profiles, the definitions used to quantify DWL anomalies, and the method of processing the acoustic data. Section 4 describes the DWL anomalies each day and observations of dissipation rate, shear, and turbulent structures within the layers. Section 5 gives the results of our analysis, comparing observed dissipation and shear to law-of-the-wall scaling, exploring layer stability and the relationship between layer-scale turbulence and elevated mixing. Section 6 synthesizes our results and discusses the implications. Section 7 summarizes the study.

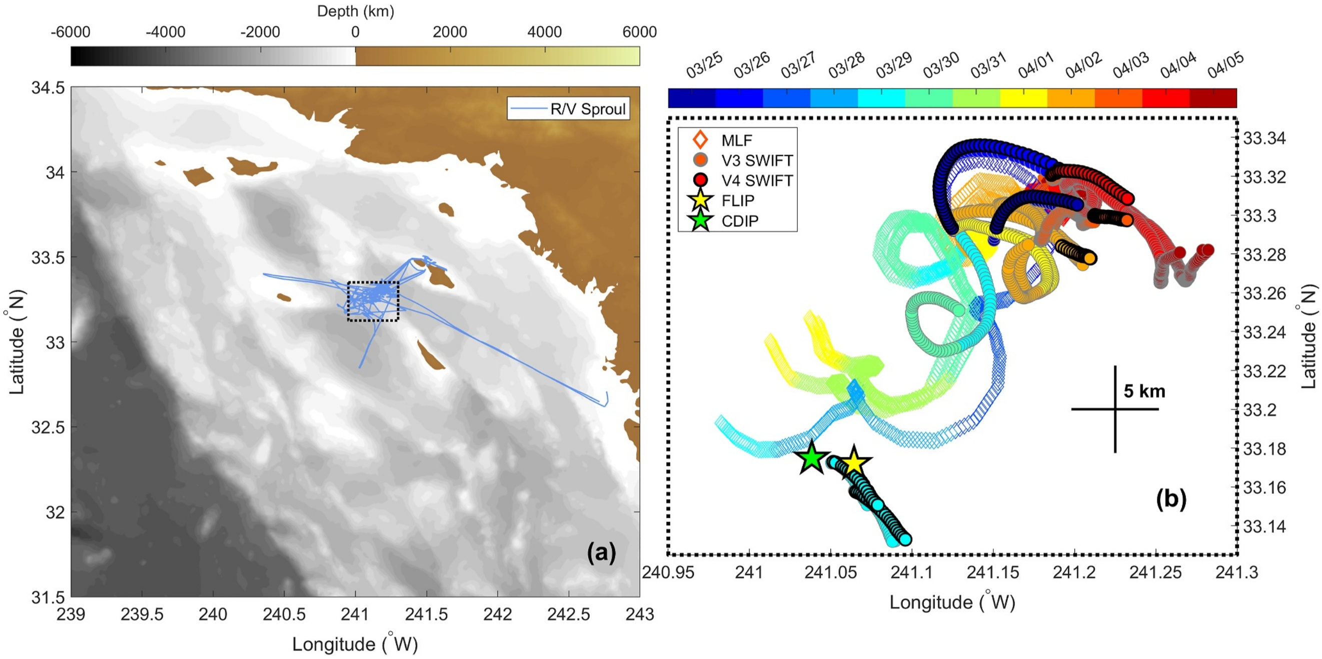

Figure 1. Location of the LCDRI experiment and instrument tracks. (a) Bathymetry overlaid with R/V Sproul ship track (blue) and outline of region where SWIFT and MLF floats were deployed (black dashed box). (b) Detail of the deployment region showing the positions of the SWIFT drifters and MLFs, as well as the location of the R/P FLIP and CDIP buoy. Colors indicate time.

2. Data

2.1. Field Experiment

The observations described in this study were collected during the Office of Naval Research "Langmuir Circulation" Departmental Research Initiative (LC-DRI) field experiment. The campaign was conducted over a 2 week period beginning in late March 2017, west of Catalina Island in the Southern California Bight (Figure 1a). Two research vessels, the R/V Gordon Sproul (RVGS) and R/V Sally Ride (RVSR), conducted surveys and repeatedly deployed and recovered autonomous and drifting instruments near the Floating Instrument Platform (FLIP), which kept station throughout the campaign. A Waverider buoy in the CDIP network (cdip.ucsd.edu) deployed 3 km from FLIP continuously measured relevant wave field parameters over the course of the campaign. Meteorological forcing variables were measured by the two research vessels as well as FLIP.

2.2. Velocity Data

Velocity and dissipation measurements were collected using "Surface Wave Instrument Floats with Tracking" (SWIFTs Thomson, 2012). SWIFTs were deployed by the R/V Sproul 10–30 km from FLIP and were typically advected ~5–10 km from their initial positions each mission (Figure 1b). By "mission," we mean each time a SWIFT was deployed to collect data and then recovered. Two versions of SWIFTs were deployed: four each of version 3 (V3) and version 4 (V4). All SWIFTs collect wave data with onboard GPS and inertial motion units (IMUs), as well as ocean temperature and salinity data from a conductivity and temperature sensor (CT) at 0.2 m depth. V4 SWIFTs were additionally equipped with down-looking Nortek Signature1000 ADCPs to measure horizontal velocities down to 20 m, and turbulent vertical velocities down to 5 m. V3 SWIFTs were equipped with sonic anemometers to measure wind speed at 1 m height. Data were collected in 8.5 min bursts every 12 min and averaged across bursts to reduce noise. V3 SWIFT missions ranged from 5 hrs to 2 days and missions lasting less than a day were always conducted during daylight hours. V4 SWIFT missions were shorter, ranging from 3 to 8 hr, typically in the afternoon. Data were collected in 8-min bursts, every 12-min and so the SWIFTs achieve a temporal resolution of 12 min.

The data which are the primary focus of this study are the high-resolution vertical velocities measured by V4 SWIFTS. As configured for this study, the ADCP (Nortek Signature1000) interleaves a long-range (LR)

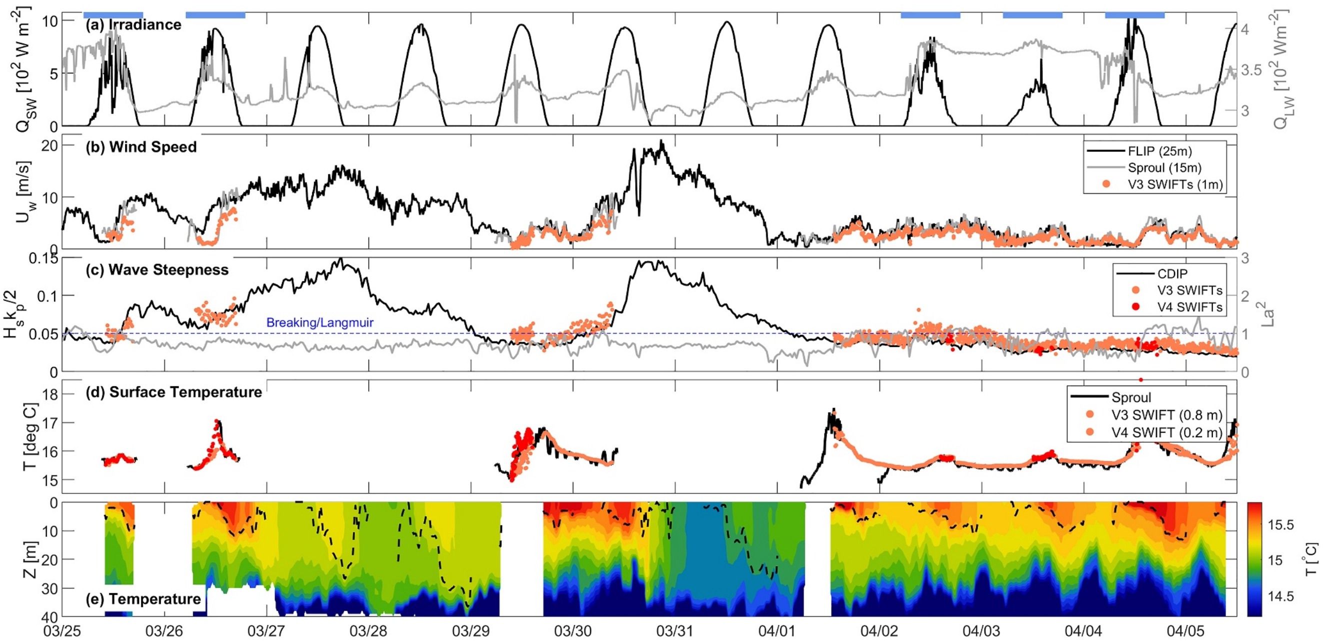

Figure 2. Atmospheric forcing variables and hydrography during the experiment from March 25 to April 05, including (a) shortwave and longwave irradiance magnitude, (b) wind speed, (c) peak wave steepness, (d) surface temperature and (e) near-surface temperature. Black and gray lines throughout indicate observations from ships and the CDIP buoy, while the colored lines and dots indicate observations from the SWIFT drifters. The blue dashed line in (c) indicates the threshold for wave breaking suggested by Banner et al. (2000). Temperature in (e) is from a single MLF. The black dashed line in (e) gives the depth of maximum stratification associated with the DWL at each time-step (Section 3.2). The blue bars at the top of panel (a) indicate the days when strong DWLs were observed which are the focus of this study. Also plotted in (c) is the turbulent La number (gray line), ranges indicated on the right vertical axis. The threshold for Langmuir turbulence (Equation 1) lies coincident with the threshold for breaking (blue dashed line).

broadband sampling mode with a high-resolution (HR) pulse-coherent sampling mode. In the broadband sampling mode, four beams in a Janus configuration sample at 1 Hz and measure horizontal and vertical velocities (and thus shear) at 0.5 m resolution down to 20 m. In the HR mode, the vertical beam samples at 8 Hz and measures along-beam (i.e., vertical) velocity profiles at 0.04 m resolution down to 5 m. Due to blanking distance and poor data quality in the first couple of bins, both the broadband and HR profiles begin at ∼0.5 m depth.

2.3. Stratification Data

DWLs were identified and characterized using temperature, salinity, and density data collected by nearby MLFs which profiled from the surface to 50 m every ∼30 min. MLFs were equipped with two conductivity-temperature-depth (CTD) sensors 1.4 m apart. MLF missions lasted a few days each and care was taken to re-deploy SWIFTs in the vicinity of the actively profiling MLFs. Relative positions of the MLFs and SWIFTs show that they were typically less than 1 km apart and no more than 4 km apart (Figure 1, inset). Temperature, salinity, and density data from individual MLFs were mapped to a regular 1 m × 30 min grid using an assumed Gaussian autocovariance of 2 m and 1 hr. Thus, velocity data is available at higher resolution (0.5 m × 12 min for horizontal velocity) over shorter periods (a few hours each afternoon) than stratification data (1 m × 30 min, all day). Direct comparisons of shear and stratification are not feasible using the SWIFT velocity measurements, due to the comparative coarseness of MLF data. However, we show ungridded stratification data (enabled by finite differencing the two CTDs on the MLFs, 1.4 m apart) to provide context for the observed shear in Section 4.3.

3. Methods

We focus our analysis on five well defined DWLs which were sampled by both V4 SWIFTs and MLFs, that is, layers for which both velocity and temperature data are available (March 25 and 26, and April 2–4, Figure 2). For simplicity we primarily show data from a single MLF (MLF83) and V4 SWIFT (SWIFT25) which obtained the best coverage over these 5 days. The observations from other SWIFTs and MLFs were similar, and our analysis is largely insensitive to the choice of specific instrument. Below we describe our method of computing surface fluxes, dissipation rate, and relative acoustic backscatter. We also provide definitions of the DWL anomalies and detail their use in computing a bulk Richardson number for each DWL.

3.1. Computing Surface Fluxes

Surface net heat and momentum flux (wind stress, τ) were computed using the COARE bulk algorithm, version 3.5 as detailed by Fairall et al. (2003). The primary dependence of momentum flux is wind speed, while heat flux also depends on air-sea temperature difference, solar irradiance and relative humidity. The algorithm additionally makes small corrections using peak wave height and period, atmospheric pressure, and precipitation if available. Continuous time series of momentum and net heat flux were obtained by applying the COARE algorithm to wind speed, air, and sea temperature measured by the RVGS, wave data measured by the CDIP buoy, and irradiance data measured by FLIP. We also compute a more "local" estimate of the momentum flux using the V3 SWIFT data, and the two estimates of τ are in close agreement. Thus we use the latter when predicting near-surface dissipation rate from Equation 3, as the V3 SWIFTs were in closest proximity to the V4 SWIFTs, which measured the dissipation rate.

3.2. Estimating TKE and Dissipation Rate

The primary purpose of the SWIFT is to measure profiles of the near-surface turbulent kinetic energy dissipation rate ($\epsilon(z)$) in a surface-following reference frame (Thomson, 2012). Our method of estimating the dissipation rate follows Zeiden et al. (2023), in which the HR along-beam velocity data are used to estimate $\epsilon(z)$ via the structure function method. Prior to computing the structure function, empirical orthogonal functions (EOFs) of along-beam velocity are used to separate turbulence from the much stronger signal due to surface gravity waves. The second order velocity structure function is then computed from the isolated turbulent vertical velocities over a limited range of separation scales ($r \leq 0.16$ m) and averaged across each 8.5-min burst, $\overline{D(z,r)} = [w(z + r/2) - w(z - r/2)]^2$, where the brackets denote ensemble averaging. The structure function may be thought of as an estimate of the turbulent kinetic energy (TKE) at the given separation scale. The ensemble average is typically estimated using temporal averaging. The burst-average structure function at each depth is then fit to the theoretical Kolmogorov curve,

$$\overline{D(z,r)} = C_\nu^2 \epsilon(z)^{2/3} r^{2/3} \tag{6}$$

to determine the depth dependent dissipation rate. Here C_ν^2 is an empirical constant, taken to be 2.1 as in Wiles et al. (2006), and the bar over D indicates a temporal average. The predicted $r^{2/3}$ dependence of the structure function is equivalent to the $k^{-5/3}$ dependence predicted by Kolmogorov theory for the turbulent kinetic energy spectrum. Thus $D(z,r)$ is an estimate of the TKE at scales r. In Section 5 we present this estimate of TKE from select bursts of ADCP data. Additional details of the dissipation rate method, processing choices and data quality control can be found in Zeiden et al. (2023).

As the structure function method is derived from an assumption of isotropic turbulence, there may be errors in our estimates of ϵ due to anisotropy in the turbulence induced by the DWL stratification. The challenge in estimating potential error is both (a) determining the scales impacted by stratification and (b) comparing estimates of ϵ with the true dissipation rate. The latter is not achievable in the field, but using numerical simulations of turbulence driven by Kelvin-Helmholtz instability, Smyth and Moum (2000) found estimates of ϵ derived from the assumption of isotropy to be accurate for values of the buoyancy Reynolds number, $\mathrm{Re}_b = \epsilon \nu^{-1} \mathrm{N}^{-2}$, O(100) and greater. Here ν is the kinematic viscosity, which has characteristic values in the ocean of 1.2×10^{-6} m^2 s^{-1}. An obvious problem with using estimates of Re_b from observations to gauge significant departure from isotropy is its circular dependence on ϵ, although we might assume sufficiently large estimates of Re_b indicate the assumption of isotropy is satisfied. In this study, characteristic values of ϵ within the DWLs are 3×10^{-7} m^2 s^{-3} and $\mathrm{N} = 0.02$ s^{-1}, which corresponds to $\mathrm{Re}_b = 625$. This is close to the threshold identified by Smyth and Moum (2000), and so is not conclusive.

However, we note that Re_b may be re-framed as a ratio of the largest to smallest scales of the inertial subrange, $(L_o/L_K)^{4/3}$. Here $\mathrm{L}_o = \left(\epsilon/N^3\right)^{1/2}$ is the Ozmidov scale, usually interpreted as the upper bound of the inertial subrange in the vertical, and $L_K = (\nu^3/\epsilon)^{1/4}$ is the Kolmogorov micro-scale at which the effects of viscosity are felt (i.e., the lower bound). The implication is that Re_b is a measure of the width of the inertial subrange in wavenumber space, and O(100) corresponds to at least a decade of separation. Here and in the literature L_K is O(10^{-1} cm) or less, even for dissipation rates 1–3 orders of magnitude smaller than characteristic of the DWL in this study. Estimates of the Ozmidov scale are more sensitive to ϵ, and range from 1 m to 4 cm for ϵ ranging from 10^{-5} to 10^{-8} m^2 s^{-3}. Here, the characteristic value of ϵ corresponds to $L_o = 0.2$ m, which is just slightly larger than the largest scale used to estimate ϵ via the structure function method above. However, a key observation of this study is of turbulent structures which span the height of each DWL, suggesting that the true upper bound of the inertial subrange is likely O(1 m). Thus, the scales used to estimate ϵ here are likely within the inertial subrange and errors induced by anisotropy are likely small.

3.3. Acoustic Backscatter Processing

Acoustic data, typically obtained with echo sounders, have been used to image turbulent flows in oceans and estuaries for decades (e.g., Farmer & Armi, 1999; Geyer et al., 2010; Moum et al., 2003). This capability is derived from the high acoustic backscatter (ABS) of regions with strong microstructure in sound speed caused by stratified turbulence compared to homogeneous/quiescent regions (Seim et al., 1995). Echo sounders measure ABS at high spatial resolution and operate over a wide range of frequencies, theoretically enabling disambiguation between signals from microstructure, bubbles, biological scatterers, sediment, and other sources (Bassett et al., 2023; Lavery et al., 2010).

Acoustic data recorded by ADCPs have not commonly been used to image turbulent flows, as they are not designed to enable calibration of the acoustic return strength and tend to be lower resolution. However, qualitative information about the structure of turbulent flows can be obtained by examining the relative acoustic backscatter strength (RABS) recorded by a single instrument (i.e., neglecting the calibrated gain). To obtain RABS as a function of time and depth for each ADCP burst, we need only correct for geometric spreading and attenuation in our signal. Following Gartner (2004), we apply a version of the SONAR equation

$$P_c = P_r + 20\log_{10}(R) + 2\alpha R + C_N \tag{7}$$

to account for range dependent attenuation and near-field effects (i.e., neglecting a constant gain offset). Here Pr is the received signal (raw ABS in dB), R is range from the ADCP, α is the absorption coefficient of sound in water (Francois & Garrison, 1982) and P_c is the corrected signal (RABS) in dB. C_N is a small near-field correction to data nearer than 0.4 m to the transducer.

It is important to note that we are unable to distinguish between different sources of scattering with ADCP backscatter data. This means periods with strong breaking waves (bubble plumes) will have high ABS returns, as will periods with ample microstructure. We show ABS observations from each DWL (Section 4.4), but focus analysis on a period when surface wave breaking was not observed and clearly periodic coherent structures are unlikely to be deep bubble plumes (Section 5.3).

3.4. DWL Anomaly Definitions

3.4.1. Temperature and Velocity

DWLs are characterized by temperature and velocity anomalies with respect to representative mixed layer values. We define the DWL temperature anomaly each day (T') to be with respect to the time-and-depth mean temperature between the surface and 10-m depth from 05:50 to 06:30 local time each morning, just before the onset of warming. Neither SWIFTs, nor MLF, nor the R/V Sproul sampled in the early morning of March 25, so we take the mixed layer temperature that day to be the minimum surface temperature observed by the R/V Sally Ride prior to warming. We define the DWL velocity anomaly (U') relative to the depth-mean velocity at each time-step, as we do not have velocity data in the early morning. We note that this definition likely underestimates the magnitude of the DWL currents as they are included in the average. The resultant DWL anomalies are presented in Section 5.1.

3.4.2. Layer Depth

The DWL depth is defined a number of ways in the literature. A commonly used definition is the “trapping depth” of the temperature anomaly given by the following equation:

$$z_T = \frac{1}{T'(0)} \int_{z_r}^{0} T'(z)dz \tag{8}$$

Price et al. (1986). Here z_r is some chosen reference depth below the DWL but above the deeper seasonal thermocline. The choice of reference depth must be done carefully to avoid bias due to internal waves moving cold water into the integration range, as often occurred in our observations (Figure 2). Here we opt for a dynamic (as opposed to fixed) z_r defined as the maximum depth of observed warming (i.e., where $T' = 0$).

A more straightforward definition of the DWL depth is the depth of maximum temperature stratification in the region above the seasonal thermocline. We define z_N as the depth of the maximum temperature gradient shallower than z_r. The dynamic range is again necessary because the strength of DWL stratification was comparable to the strength of the seasonal thermocline and there was no fixed depth which reliably separated the two. The resultant z_N and z_T values were highly correlated (0.9), but z_T was on average 3 m deeper than z_N. This is likely because the gridded temperature product underestimates the true surface temperature $T'(0)$. As we are primarily concerned with the relationship between shear, stratification and mixing in this study, we use z_N to indicate the DWL depth.

3.4.3. Bulk Layer Differences

As noted in Section 2.3, raw stratification data at depth were coarse compared to velocity data, and direct (point-to-point) comparison of shear and stratification is not possible. To gauge layer stability we instead compute the bulk Richardson number (Equation 5). We take the layer depth H to be z_N as stated above. We assume stratification is set by temperature, and estimate ΔT across the layer using the 0.2 m “surface” temperature measured by the SWIFT drifter and the mean ungridded MLF temperature 5 m below z_N at each time step. This approximation is necessary because temperature profile data from the MLF are too coarse and therefore the gridded product substantially underestimates the peak surface temperature. The layer density difference is then obtained by approximating $\Delta\rho = \alpha_T \Delta T$ where α_T is the linear thermal expansion coefficient equal to -0.23 kg m^{-3} $^{\circ}\mathrm{C}^{-1}$. We similarly estimate ΔU to be the mean relative velocity (in the drifting reference frame) measured by the SWIFT ADCP 5 m below z_N. In other words, the mean relative velocity at depth gives the velocity difference across the layer. Resultant Ri_b for each DWL are shown in Section 5.2.

4. Observations

We begin with an overview of the forcing and surface conditions during the period when DWLs were observed. The remainder of the manuscript focuses on the 5 days when strong DWLs were sampled by both MLF and V4 SWIFTs, for which both stratification and velocity data are available (March 25 and 26, April 2–4). We follow with details of the DWL anomalies these days, namely temperature and velocity. We then show observations of dissipation rate and shear within the DWLs measured by the V4 SWIFTs. Finally we show images of relative acoustic backscatter from select ADCP bursts each day, which indicate the presence of coherent structures within the DWLs. Analysis and discussion of these observations are reserved for Sections 5 and 6.

4.1. Surface and Forcing Conditions

Over the course of the experiment, atmospheric, and surface conditions were highly variable (Figure 2). Skies were clear most days and incoming shortwave solar radiation peaked around 1,000 Wm^{-2} at midday. Two overcast days had peaks of ~ 500 W m^{-2} (April 2 and 3). Wind forcing from March 25 through April 1 was dominated by two events with peak 10-m wind speeds exceeding 15 m s^{-1}. These were followed by a calmer period between April 1–6, when wind speeds were predominantly below 5 m s^{-1}. Significant wave height (H_s) was up to 4 m during both wind events, and peak wave periods were ~ 8 s (not shown).

During calm periods H_s was less than 2 m and peak wave periods were 10–12 s. Corresponding wave steepness ($H_s k_p/2$) during the two wind events exceeded the breaking threshold of 0.05 (as suggested by Banner

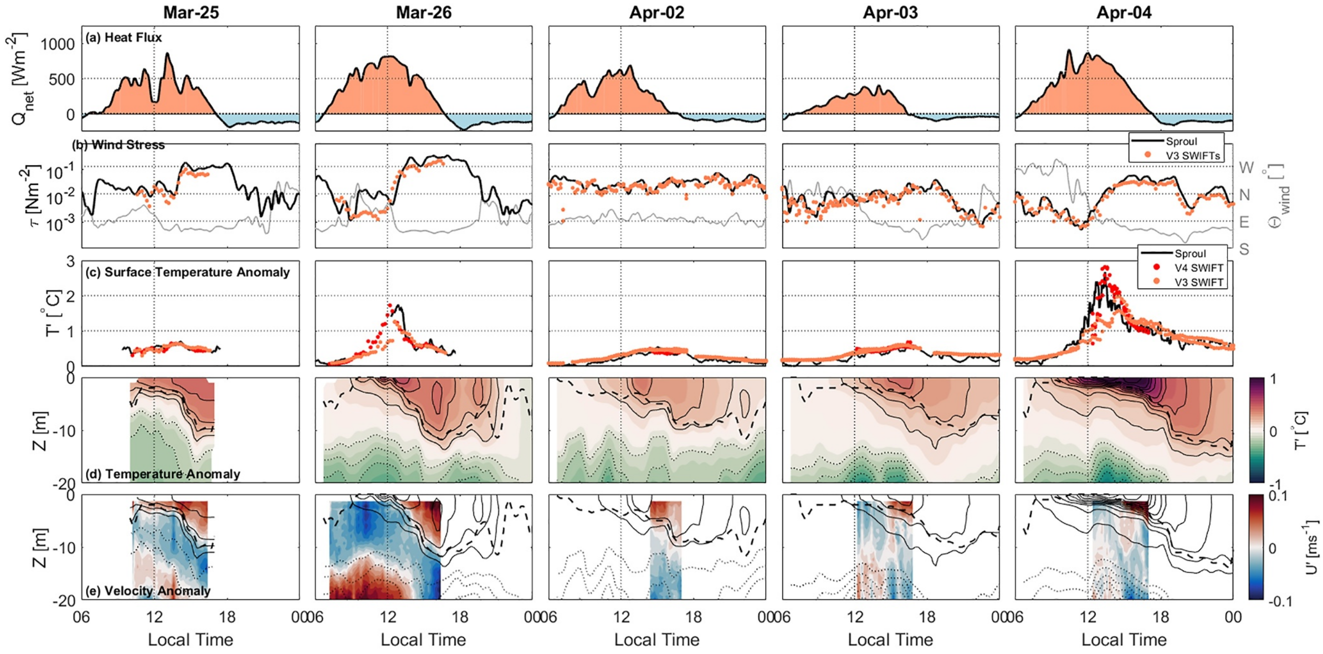

Figure 3. Evolution of surface forcing and diurnal warm layer development during the observation period. Shown are (a) net surface heat flux, (b) wind stress and wind direction, (c) surface temperature anomaly, (d) near-surface temperature anomalies, and (e) downwind velocity anomaly on the 5 days DWLs were observed by both V4 SWIFTs and MLFs. Black lines in (b) show wind stress estimated from R/V Sproul wind speeds. The dashed black line in (d) and (e) indicates the depth of maximum stratification, and black contours are 0.1°C temperature anomaly intervals.

et al. (2000), blue line in Figure 2c), indicating widespread breaking during these storms. In contrast, little breaking could be expected during the calm period in April. A similar pattern in the turbulent Langmuir number, La, suggests conditions were ripe for Langmuir turbulence during the two storms in March but may not have occurred during the calmer period in April (gray overlay in Figure 2c). La, which weighs wind-forced against wave-forced turbulent production, is given by La$= \sqrt{u_*/u_S}$ (Belcher et al., 2012). Here $u_* = \sqrt{\tau/\rho_w}$ is the water-side friction velocity and $u_s = \omega k (H_s/2)^2$ is the Stokes drift, τ is the bulk estimate of the local wind stress (from FLIP wind speed, see Section 3.1 for method), ρ_w is the representative water density, and ω and k are the peak wave frequency and wavelength, respectively, from the nearby CDIP buoy. Langmuir turbulence is likely to occur when La^2 is less than 1, that is, when wave forced production likely exceeds wind-forced production. Consistent with this interpretation, in another study from the same experiment, Grare et al. (2018) observed temperature cells consistent with Langmuir turbulence during the March-30 storm from temperature sensors suspended from a Waveglider which surveyed near both platforms. Together the breaking and Langmuir parameters suggest wave breaking and Langmuir turbulence may have driven upper ocean TKE during the two storms, but were not likely to be the dominant mixing mechanism during the calm period in April.

Diurnal surface warming was evident most days, highlighted by midday maxima in near-surface temperature (Figure 2d). Warm layers were initially shallow but deepened throughout the day, reaching depths of ~10 m within an otherwise homogeneous mixed layer about 35 m deep (Figure 2e). Here we have estimated the depth of the mixed layer to be the mean depth of the maxima in stratification below 15 m depth (to distinguish from the maxima associated with the DWL) at each time step during the observation period (roughly corresponds to the 14.5° temperature isotherm in Figure 2e). Each night the mixed layer was homogenized, presumably due to convection driven by nighttime surface cooling (see Figure 3a for the evidence of the heat flux becoming negative in the evening). During both wind events, warming was weak and the surface layer remained well mixed down to the base of the mixed layer.

4.2. Diurnal Warm Layer Characteristics

Surface forcing and resultant temperature and velocity anomalies varied substantially across the five DWL events observed by both SWIFTs and MLFs: March 25, 26, April 2, 3, and 4. Generally, surface warming (net positive heat flux) began at 06:30 local time (LT) each day, peaked just prior to 12:00 LT and switched to cooling (net negative heat flux) at ~17:00 (Figure 3a). On April 3 peak warming did not occur until 14:00 LT, then rapidly switched to cooling at 16:00 LT. Wind stress followed two distinct patterns: (a) steady moderate/weak wind speeds throughout the day on April 2 and 3, and (b) weak morning winds followed by strong winds in the afternoon on March 25, 26, and April 4 (Figure 3b). The latter is indicative of a diurnal sea breeze, where onshore winds (here eastward) develop each afternoon due to an ocean-land temperature differential which builds throughout the day. On all three sea-breeze days, wind stress increased by an order of magnitude around 12:00 local time. Wind stress estimates from the nearby RVGS generally agreed with the SWIFT drifters, except on March 26 when they differed by an order of magnitude in the AM. The reason for this discrepancy is not clear, as the distance between instruments was no greater on March 26 than other days.

Surface temperature anomalies $\left(T'\right)$ each day were strong, especially on March 26 and April 4 when peak surface warming reached 2 and 3°C, respectively (Figure 3c). Weaker peak T' of ~0.5°C on March 25, April 2 and April 3 were more representative of previous DWLs observed under similar forcing conditions (e.g., K. Hughes et al., 2021; Moulin et al., 2018; Sutherland et al., 2016; Wijesekera et al., 2020). In general, early morning warming was confined to the upper few meters but extended throughout the day, reaching maximum depths of ~10 m around 20:00 LT before being homogenized in the evening (Figure 3d).

Each day surface warming was accompanied by the development of a downwind velocity anomaly $\left(U'\right)$ within the DWL (Figure 3e). Here velocity has been rotated into a coordinate system defined by the mean wind direction from 12:00 to 18:00 LT each day, which was weakly south of east (gray line in Figure 3b). The surface flow is clearly accelerated in the downwind direction each day, with the current depth bounded by the DWL stratification. At the surface, velocity anomalies were O(0.1 m s^{-1}), consistent with previous observations (e.g., Sutherland et al., 2016; Wijesekera et al., 2020).

4.3. Dissipation Rate and Shear

Profiles of TKE dissipation rate (ϵ) suggest that wind-driven turbulence was modulated by DWL stratification each day (Figure 4). Dissipation rates were strongest on March 26 when the diurnal sea breeze exceeded 10 m s^{-1}, and weakest on April 03 when wind speed was consistently below 5 m s^{-1}. Within each layer, ϵ ranged from 10^{-7} to 10^{-5} $\mathrm{m}^2\mathrm{s}^{-3}$, was strongest near the surface and decreased gradually with depth. Here and throughout the rest of the manuscript, by "within the layer" we mean above the base of the DWL as designated by the dashed black line. Across the base of the layers, ϵ generally dropped an order of magnitude to 10^{-8} $\mathrm{m}^2\mathrm{s}^{-3}$. Contours of ϵ emphasize strong vertical and temporal gradients at the base of the DWLs and in time (contour lines in Figures 4b–4d). For example, the strongest at-depth gradients in ϵ were observed around 14:00 LT on March 25, 26, and April 4 when those DWLs deepened rapidly with the development of the afternoon sea-breeze.

Interestingly, ϵ within each layer decreased to sub-layer values when the local wind speed dropped to or below 2 m s^{-1}. This can be seen just before 12:00 and 14:00 LT on March 25, and 16:00 LT on April 03. There is support in the literature for a wind-speed threshold for DWL mixing. From the 1D momentum and heating equations, K. Hughes et al. (2020) showed that wind speeds must exceed ~2 m s^{-1} for active overturning to occur. Though we do not observe the upper 1 m, our observations appear to provide support for this threshold. The exact value varies slightly depending on heating time scale and latitude, though values used by K. Hughes et al. (2020) are similar to those here.

An important characteristic highlighted by Figure 4 is that the strongest DWL ϵ values were not coincident with the strongest shear values. Instead ϵ decays sharply across the regions of strongest shear, which occurred near the base of the DWL each day (Figure 4c). Two modalities were apparent. Shear was about twice as strong on days with an afternoon sea-breeze and strong stratification, with a distinct maxima at depth near the base of the layer (March 25, 26, and April 4). On the other 2 days (April 02 and 03) under weaker wind forcing, the shear maxima were modest and more diffuse across the DWL base (see note at the end of this section regarding the alignment of the DWL base and shear). Although we are unable to calculate a fine-scale Richardson number to evaluate the stability within these strong shear regions, point estimates of N suggest comparably strong stratification may have suppressed turbulence at the base (Figure 4d). This is consistent with the rapid decrease in ϵ at the depth of the S and N maxima.

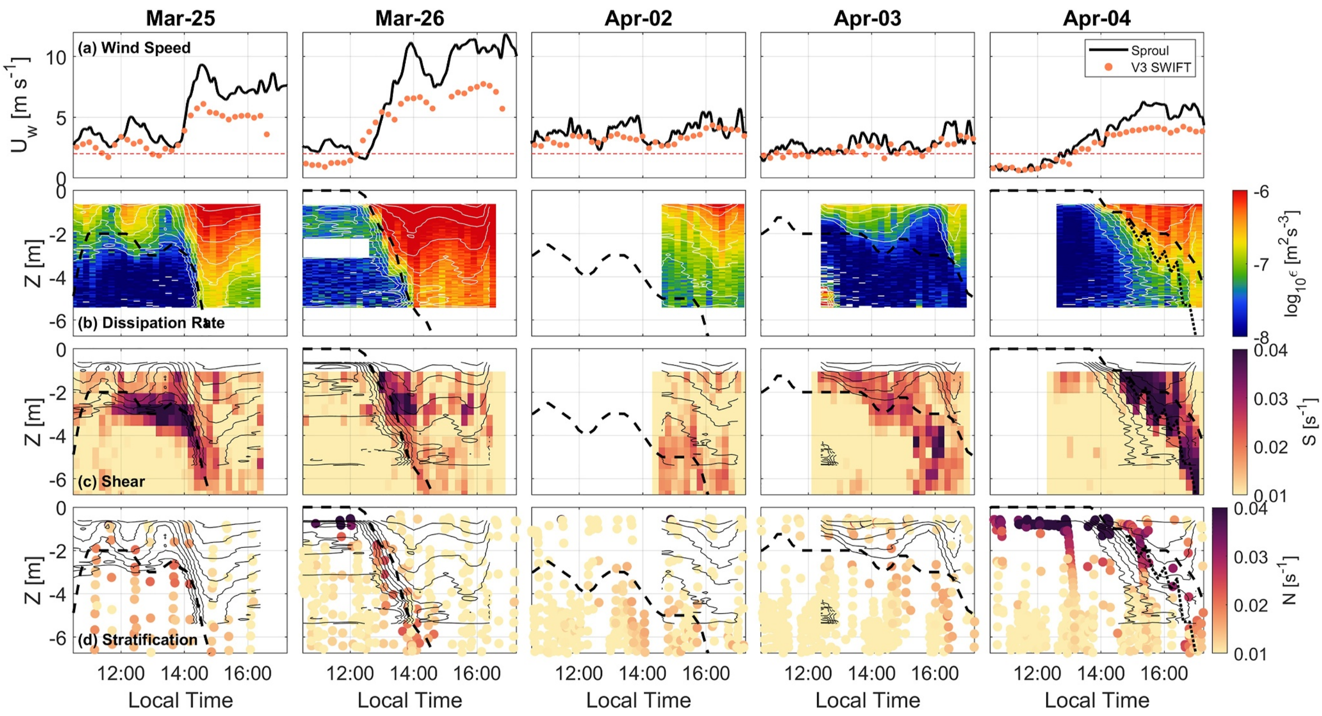

Figure 4. (a) Wind speed, (b) dissipation rate and (c) shear measured by the SWIFT within the DWLs, and (d) stratification measured by the MLF. White lines in (b) and black lines in (c) and (d) are smoothed (in log space) contours of dissipation rate ranging from −7.5 to −5 in intervals of 0.2. Dashed black lines in (b)–(d) give the depth of the DWLs as defined by the maxima in N^2. On April 4, the dotted black line additionally shows the depth of maximum shear, as this day is examined in detail in Section 5. Stratification and shear are not well aligned on April 03 and 04 likely due to the comparatively sparse MLF sampling apparent in (d).

We note on April 3 and 4, after 14:00 LT the maxima in shear appears to fall below the base of the DWL as defined by the gridded MLF product (the dashed black lines in Figures 4b–4d). This offset is likely due to error in the gridding process introduced by the comparatively coarse MLF vertical sampling. Point estimates of N (i.e., the ungridded MLF data) suggest the maxima in stratification is in fact well aligned with the maxima in shear on both of these days.

4.4. Coherent Structures

Time-depth images of relative acoustic backscatter (RABS) from select ADCP bursts each day reveal coherent structures spanning the depth of the DWLs (Figure 5). Here we describe these observations, reserving further analysis for Section 5.3 and discussion of their dynamics for Section 6. Bursts were selected to showcase the growth of structures in each DWL as they deepened, so they occur at different times but span ~2 hr each day. As with shear and dissipation rate, two modalities of wind forcing are reflected in the character and evolution of the structures. On the three sea-breeze days when the DWLs underwent a period of rapid growth (March 25, 26, and April 4), structures were roughly bound by the layer depth and exhibited at least some degree of periodicity. This was clearest on March 26 and April 4 when morning wind speeds were below 2 m s^{-1}, surface warming exceeded 1°C, and the base of the DWLs was highly stratified. On the 2 days with constant wind forcing and gradual DWL growth (April 2 and 3), the character of coherent structures did not vary substantially over the 2 hr window. On April 2, structures were highly intermittent and variable in depth. Structures were absent on April 3 when the weakest DWL dissipation rates were observed.

Corresponding images of turbulent kinetic energy (TKE) reveal a clear relationship between coherent structures within the DWL and strong turbulence (Figure 6). Here TKE is estimated as the mean value of the velocity structure function over the same scales used to determine the burst-averaged value of ϵ, and so is not the full TKE (Section 3). Although noisy, patches of enhanced TKE are clearly bound by contours of RABS. Because turbulent density microstructure produces high acoustic returns, the relationship between backscatter and TKE is not surprising. It is not a given though, as bubbles may also cause high acoustic returns. Bubble plumes generated by

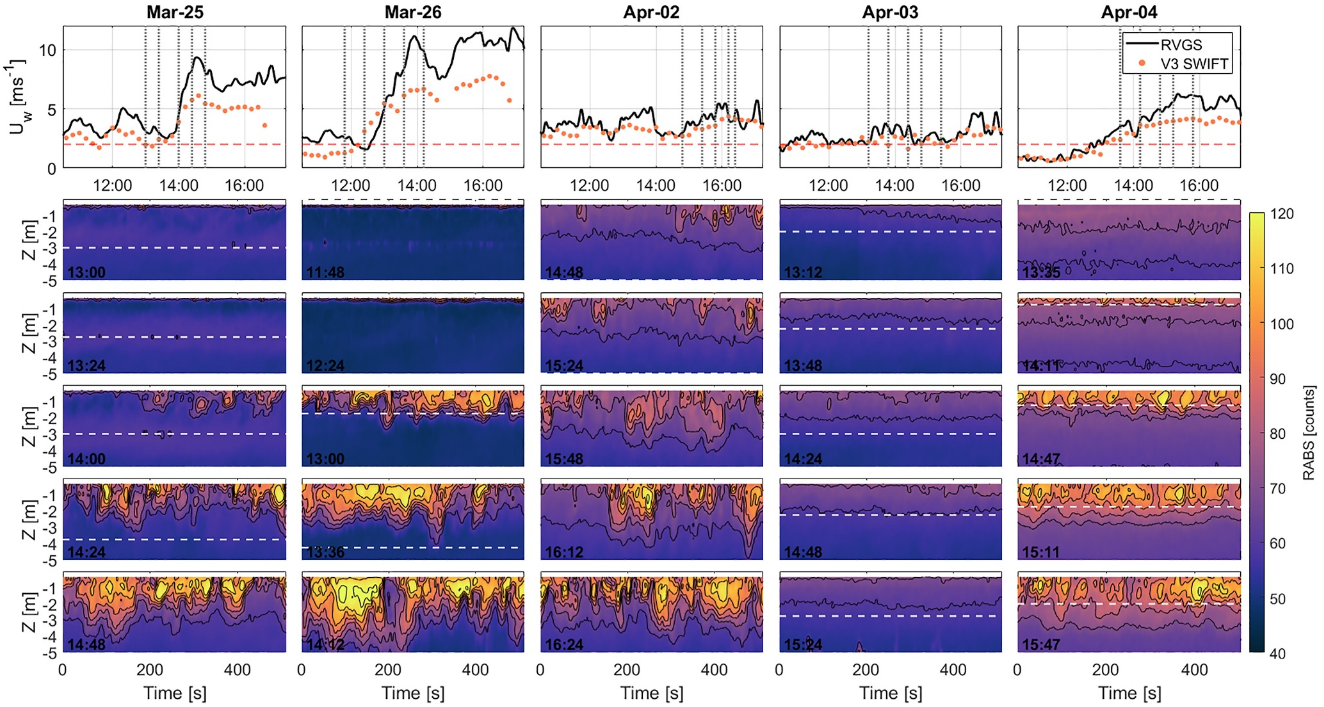

Figure 5. Time-depth images of relative acoustic backscatter (RABS) from five select ADCP bursts (rows) on each day (columns). The timing of the bursts is indicated with gray vertical lines on the same time series of wind speed and surface temperature anomaly as Figure 4 (top row). Each burst is 512 s (8 min). The depth of the layer at the time of each burst is marked with a white dashed horizontal line. Except for April 3, structures developed near the surface each day and grew in intensity and scale as the DWLs deepened.

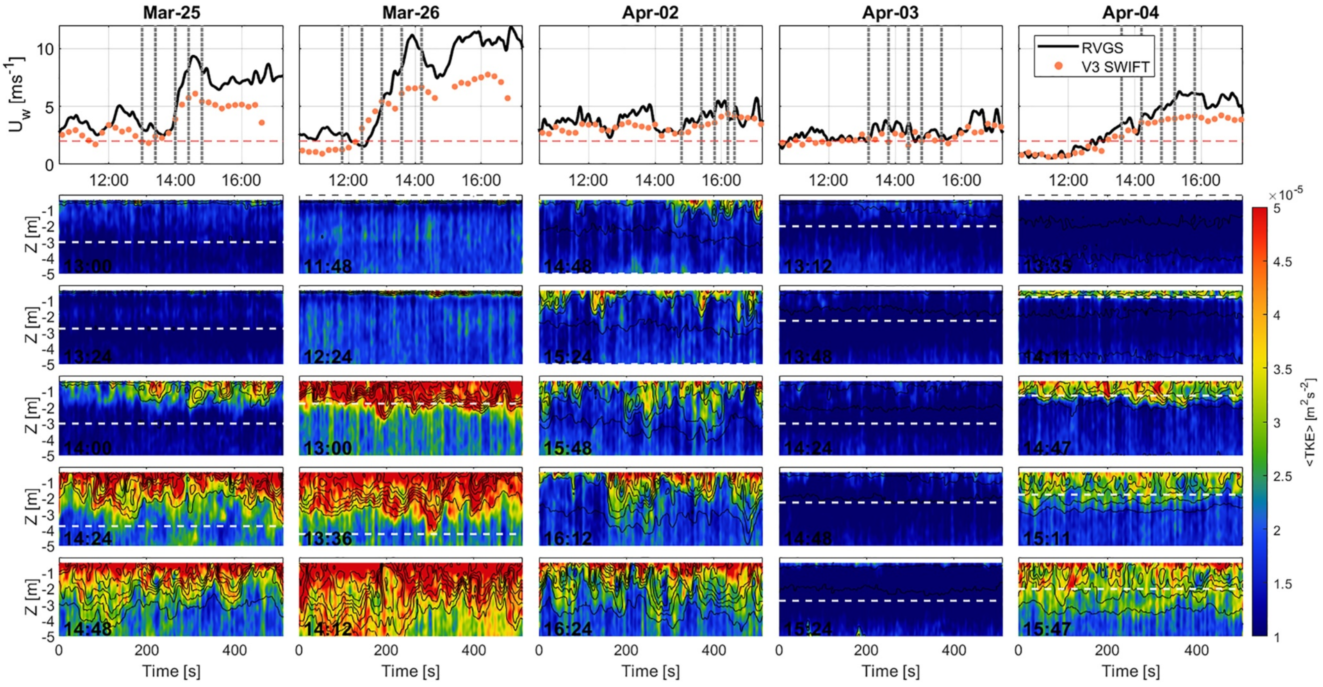

Figure 6. As in Figure 5, but for turbulent kinetic energy (TKE).

breaking waves are a plausible source of strong ABS and have been linked to elevated turbulence levels (Derakhti et al., 2020). Estimates of wave steepness each day suggest breaking was only plausible on March 25 and 26 (Figure 2c). Bubble plumes generated by breaking waves are expected to be ~ 1 m for wind speeds less than 5 m s^{-1} (Derakhti et al., 2023), and plume depths reaching 5 m require wind speeds of ~ 10 m s^{-1}. However, turbulent Langmuir numbers (La^2) consistently below 1 (on average 0.5) during both storms in March suggest Langmuir circulation (LC) may have been present on those days (Figure 2c). In a recent study of Langmuir turbulence using an AUV equipped with an uplooking Signature1000 ADCP (the same instrument used to image turbulence by SWIFTs), Fisher and Nidzieko (2024) observed periodic structures in acoustic backscatter which they attributed to bubble plumes entrained by LC. It is plausible LC similarly entrain bubble plumes to depths greater than 1 m on March 25 and 26 in this study. Regardless, during the calmer period in April, wave breaking and Langmuir turbulence are not suggested by the Langmuir and breaking parameters. Thus, while the coherent structure of high ABS regions may be attributable to bubble plumes on March 25 and 26, they do not likely explain the coherent structures observed in April. Whether due to bubble plumes or small-scale turbulence, these observations show coherent structures strongly modulate elevated DWL TKE. This relationship suggests that layer-scale structures either advect elevated turbulence from the very near-surface down through the base of the stratified layer, or are a source of fine-scale turbulence themselves, or both.

5. Analysis

In the following analysis, we first compare observed dissipation rates with law-of-the-wall scaling and show that ϵ is elevated with respect to ϵ_τ (Equation 3). We explore whether substitution of the observed shear improves predictions, but find similar enhancement. We proceed to evaluate the stability of the layer with estimates of the bulk Richardson number (Equation 5), which suggest a decrease in stability each afternoon. Finally, we attempt to elucidate the velocity and turbulence characteristics of the periodic structures observed on April 4 by averaging the data as a function of phase.

5.1. Modulation of Dissipation Rate

Here we compare observed ϵ with the two simple predictions discussed in Section 1: the law-of-the-wall scaling model (ϵ_τ, Equation 3) and shear-production model using the observed shear and an assumed linear decay profile for the turbulent stress (ϵ_S, Equation 4). For plotting purposes, we impose an approximate background level of 10^{-8} m^2 s^{-3} in the latter where the stress goes to zero below the DWL depth, based on the minimum values of observed ϵ at depth (Figure 4).

Consistent with previous studies, observed dissipation rates were elevated compared to ϵ_τ within the DWLs and suppressed below (Figure 7). The exception was when wind speeds dropped below 2 m s^{-1}, providing further support for the mixing threshold predicted by K. Hughes et al. (2020). Averaged across time and depth within the DWL, across all 5 days, ϵ was 4.7 times greater than ϵ_τ. This may not be the most meaningful metric, as the distribution of dissipation rates here and in the literature is approximately log-normal (Gargett, 1999). An alternative metric is $\log_{10}(\epsilon/\epsilon_\tau)$, as visualized in Figure 7d. This value is 0.25 on average within the DWLs, which corresponds to a difference between ϵ and ϵ_τ of 78%. When averaged over the full observation depth range (i.e. down to 5 m), the difference between ϵ and ϵ_τ decreases to 17%. This comparison reinforces previous results that the surface energy flux is likely well predicted by the wind stress to first order, though we cannot close the budget without observations from the surface to the mixed layer depth (Thomson et al., 2016; Zippel et al., 2022). The difference between observed and predicted dissipation rates within the DWL was greatest on the morning of March 25 and afternoons of April 3 and 4 (i.e., large values of $\log_{10}(\epsilon/\epsilon_\tau)$), suggesting the presence of strong shear at the base of the DWL is related to elevated ϵ throughout the layer. Dissipation rates within the DWLs were closest to the predicted value in the afternoon of March 25 and 26 when strong afternoon sea breezes came on rapidly, possibly indicating different processes driving turbulence production on those days. As noted in Section 4.4 wave breaking was likely on March 26 and later in the afternoon on March 25, so it may have been the dominant mixing process on those days. A striking feature of the comparison between observed and predicted dissipation rates is the relative uniformity of the difference within each layer despite strong gradients in shear and stratification (Figures 4c and 4d). This suggests the processes driving elevated dissipation occur throughout the layer, and are not concentrated at the boundary. This description is consistent with both bubble plumes and shear instabilities which overturn at the scale of the layer.

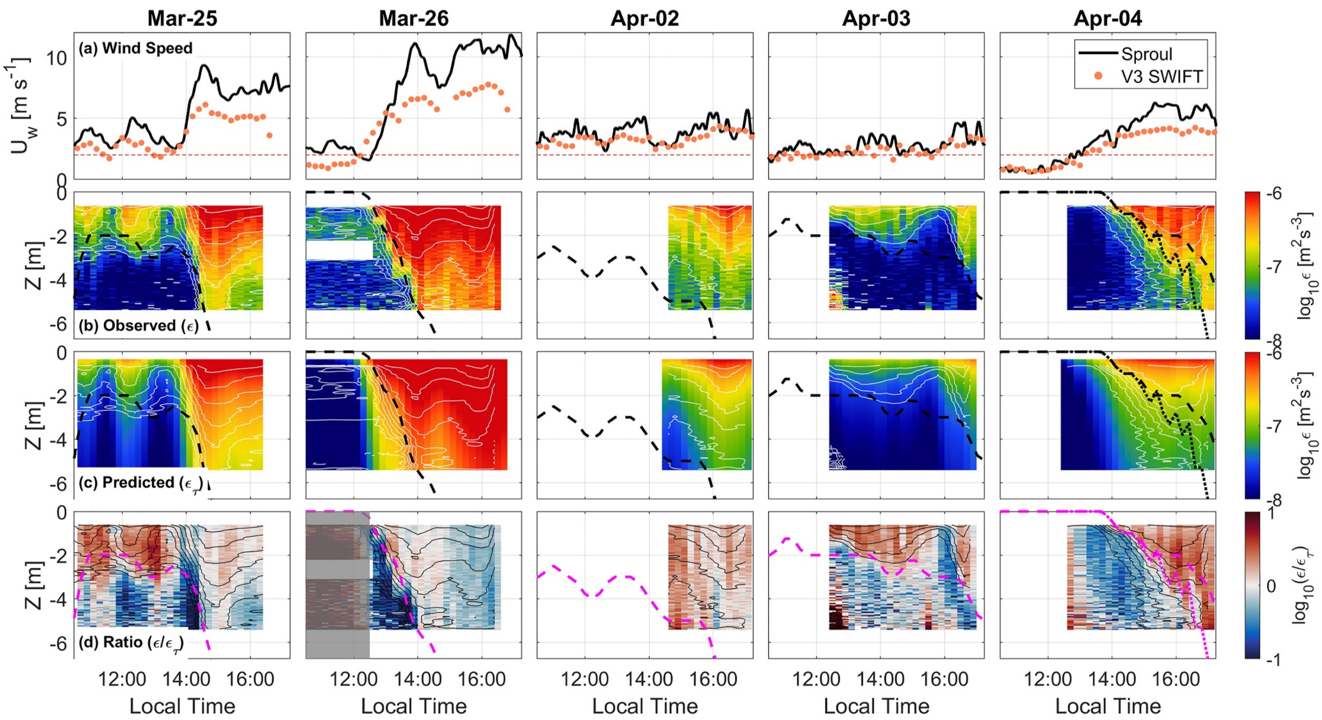

Figure 7. Comparison between TKE dissipation rate measured by SWIFT drifters (ϵ) and estimated from law-of-the-wall scaling using the observed wind stress $\left(\epsilon_\tau = -u_*^3/\kappa z\right)$. Row (a) is wind speed from both the SWIFTs and nearby R/V Sproul, row (b) is observed dissipation rate, row (c) is wind-predicted dissipation rate, and row (d) is the ratio of observed to predicted. Dashed lines in (b)–(d) indicate the layer depth as given by z_N. On April 04, the dotted lines indicate the depth of maximum shear.

Profiles of shear and dissipation rate scaled by the layer depth and law-of-the-wall predictions reinforce the picture of elevated mixing within the layer, which is bounded by strong shear at the base (Figure 8). Dimensional profiles emphasize the strong gradients in ϵ through the base of the deepening DWL coincident with enhanced shear (Figures 8a and 8b). Scaled ϵ profiles emphasize the persistent and relatively uniform proportional enhancement/suppression of turbulence above/below the layer. Scaled shear profiles show progressive enhancement of shear relative to law-of-the-wall scaling at the base of the layer over time (Figure 8d).

Using the shear-production scaling (i.e., ϵ_S, Equation 4) on average improves predictions of TKE dissipation within the DWLs (Figure 9). At different times the scaling both over and under-predicts ϵ, but on average the logarithmic ratio of ϵ to ϵ_S was 0.15 (i.e., ϵ 41% stronger than ϵ_S). We note that the ratio of ϵ to ϵ_S is noisy, likely in part due to the disparate resolutions of ϵ and S. A clear weakness of the model is its inability to predict ϵ below the DWL depth and its strong sensitivity to the prescribed layer depth. Here our assumption of a constant background value of dissipation (10^{-8} m^2 s^{-3}) strongly under-predicts ϵ below the layer on March 26 and April 04, and generally within a few 10s of meters of the DWL base. The result is that while the shear production scaling improves the prediction within the layer, when averaged across the full observation range (down to 5 m) observed ϵ is on average 54% stronger than ϵ_S. Thus for an integrated quantity, such as the total energy flux, law-of-the-wall scaling might provide better predictions. Otherwise a more complicated model for the stress profile below the layer is required (e.g., Stokes et al., 2024).

5.2. Layer Stability

The combined observations of elevated dissipation rates throughout the DWL and coherent, layer-scale turbulent structures suggests overturning of the layer may be a source of turbulence in the DWL (Figures 4 and 5). Here we compute the bulk Richardson number for each DWL to gauge whether this is a reasonable interpretation. Each day the evolution of Ri_b followed one of two patterns (Figure 10c). On March 25, 26, and April 4 under variable wind stress forcing, Ri_b was high in the late morning/early afternoon (>0.65, stable) and then decreased in the afternoon (<0.65, unstable). A clear peak in Ri_b was apparent on March 26 and April 4 when the layer velocity difference

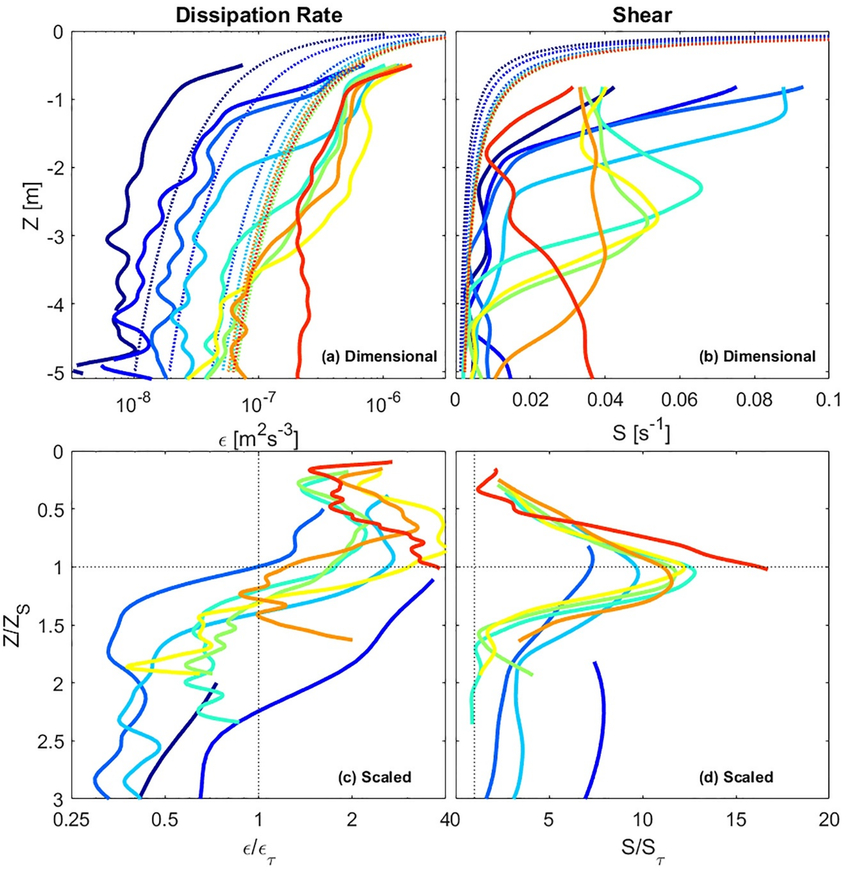

Figure 8. Profiles of observed dissipation rate and shear on April 4 at discrete times throughout the day (intervals of 30 min, blue colors are earlier). (a and b) Give dimensional profiles of ϵ and S (solid lines), along with their law-of-the-wall predictions (dashed lines), while in (c) and (d) ϵ and S are scaled by their law of the wall predictions, and z is scaled by the DWL depth. The scaled profiles emphasize elevated ϵ within the layer, suppression below, and enhanced shear coincident with the layer base.

was at a minimum, just prior to the maxima in surface temperature anomaly. On April 2 and 3 under constant wind stress, Ri_b was unstable at all times (although we note observations did not start until almost 15:00 LT on April 2). While the precise timing of the transition from stable to unstable was somewhat sensitive to how we chose to define the layer thickness and differences (as well as uncertainty in the appropriate critical value), the qualitative patterns in Ri_b evolution were not.

Broadly, the evolution of Ri_b on March 26 and April 4 suggests the onset of overturning within the DWLs may be responsible for the sudden erosion of strong T' at the surface, possibly due to elevated mixing. Low values of Ri_b are expected to result in downward growth of the DWL by entrainment of colder, deeper water from below, with subsequent cooling of the warm layer. On both days, Ri_b reached a maximum value (maximum stability) about 30 min before peak T' was observed. That is, stability of each DWL began decreasing even as the temperature difference between the two layers continued to build. These results are consistent with the dynamic cycle described in previous studies; stratification develops due to differential heating in the early morning, which in turn supports the development of strong shear within the DWL (Wijesekera et al., 2020). Shear increases as momentum builds within the layer, decreasing the stability of the layer (e.g., K. Hughes et al., 2021; Moulin et al., 2018; Price et al., 1986). At some juncture, the conditions exist for overturning on the layer scale which quickly erodes the strength of the temperature anomaly at the surface.

However, these results do not indicate a clear Ri_b threshold for instability. For example, on March 26 the layer begins to deepen while Ri_b is well above 0.65, while on March 25 deepening does not begin until about 14:00 LT, although Ri_b is nearly 0.25 for 1 hr prior. A difficulty in interpreting the bulk Richardson number is that it assumes constant shear and stratification throughout the layer. We have repeatedly noted the offset between shear and

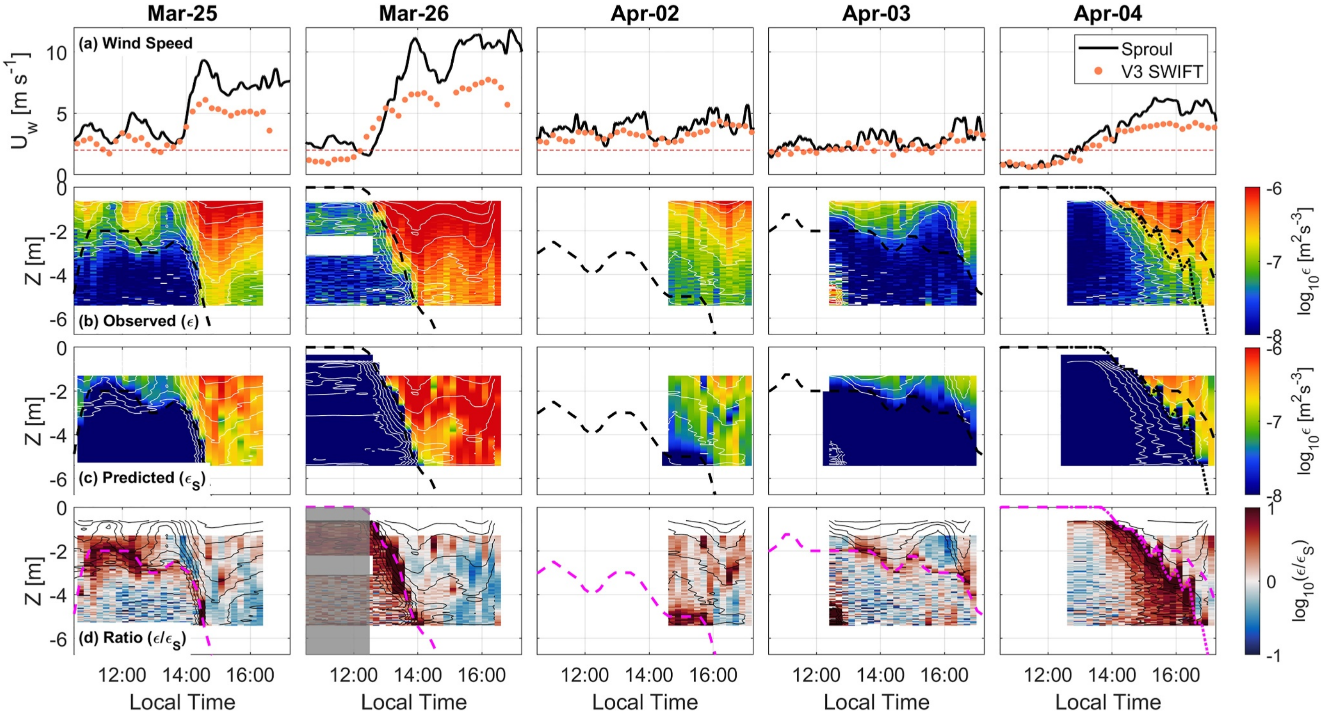

Figure 9. As in Figure 7, but for the shear-production scaling given by Equation 4.

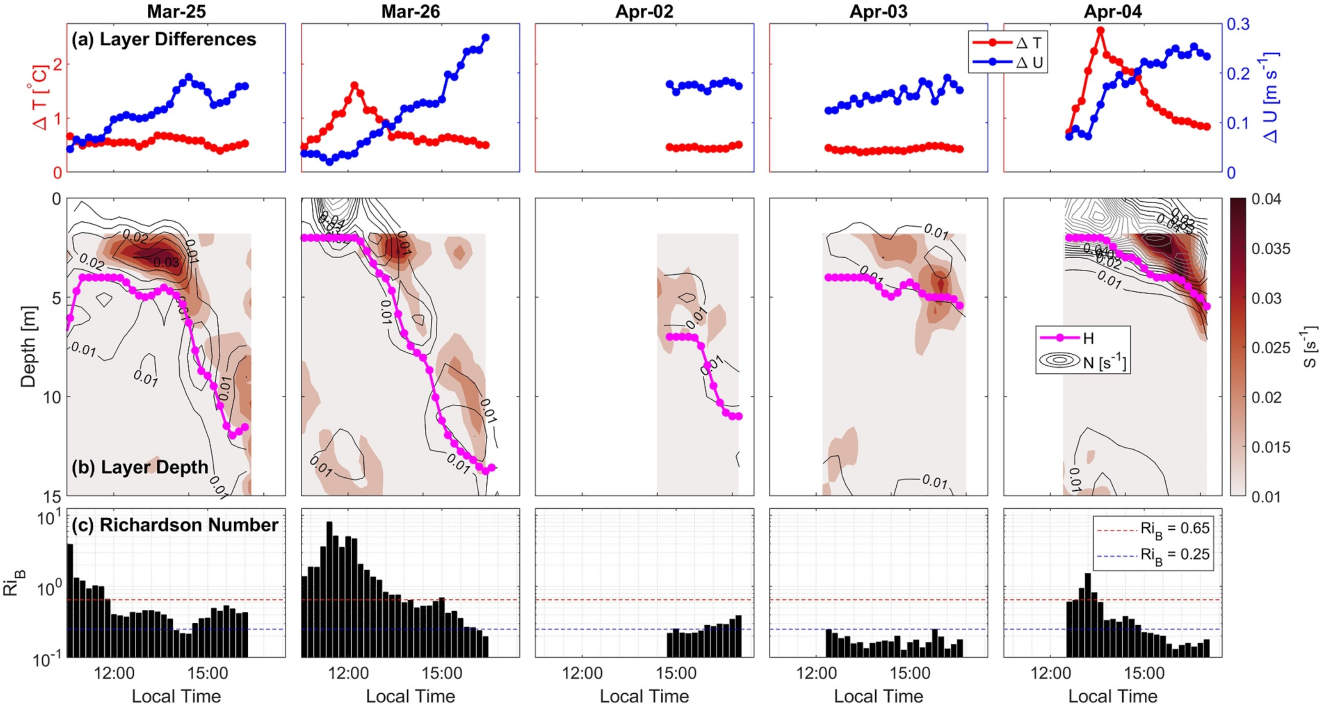

Figure 10. Layer stability evaluated using the bulk Richardson number (Equation 5). Shown are (a) temperature and velocity difference across the layer (blue and red lines, respectively), (b) shear and (c) Ri_b for each DWL. Details of the calculation can be found in Section 3.4. The pink line in (b) shows the layer depth, while the dashed red and blue lines in (c) indicate Ri_b equal to 0.65 and 0.25, respectively.

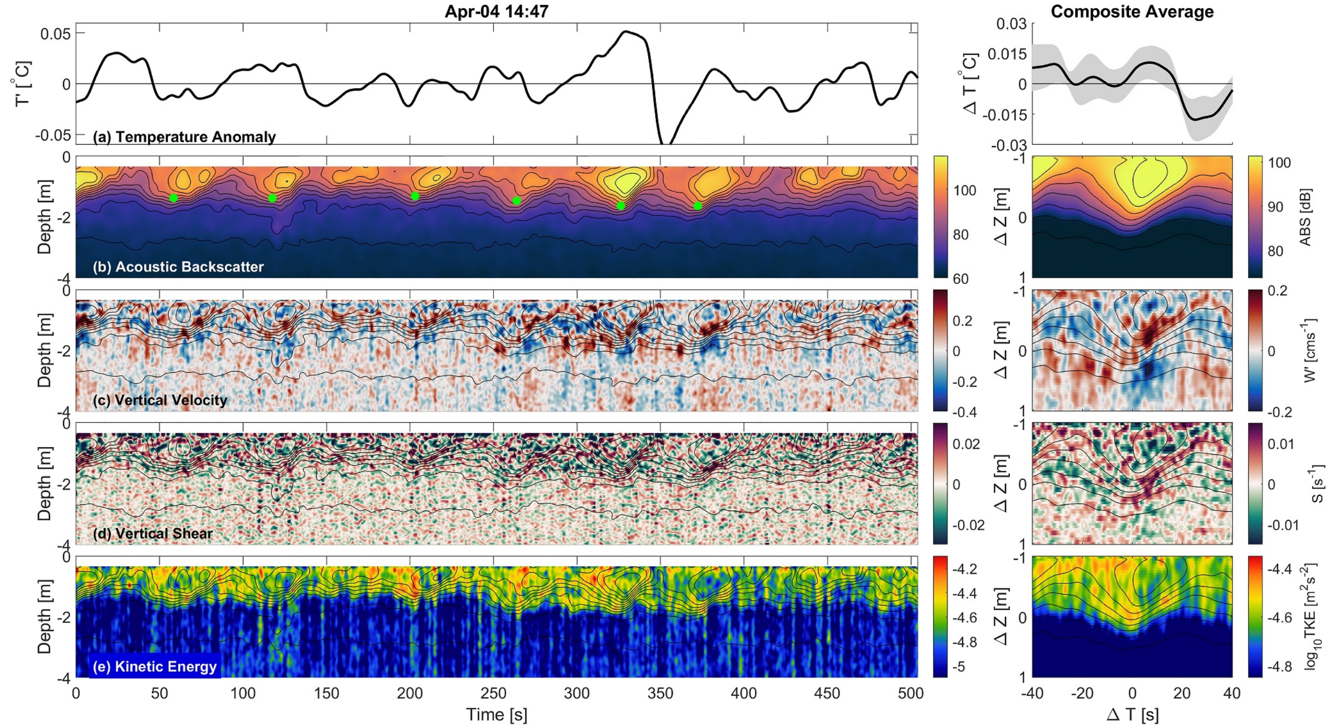

Figure 11. Averaging with respect to phase of the coherent structures identified at 14:47 LT on April 4. Shown are (a) temperature, (b) RABS, (c) turbulent velocity, (d) vertical velocity gradient, and (e) turbulent kinetic energy. Phase-averaged values are shown to the right. Individual structures are identified by depth maxima in the RABS contour whose mean position corresponded to the DWL depth (red dots in (b)). Black contours in all panels are of RABS.

strong mixing, due to the concentration of shear at the base of the DWL. By taking the velocity difference to be between the surface and just below the layer, we are effectively distributing the shear at the base throughout the layer. It is unclear whether the interpretation of overturning in the layer holds for low Ri_b across a non-constant shear layer.

5.3. Conditionally Averaged Turbulence

The highly periodic coherent structures observed on April 4 provide us with an illustrative case study of the character of layer-scale turbulent structures in a DWL, which are not readily attributable to bubble plumes generated by wave breaking. Here we examine the burst of data at 14:47 LT when structures were strongly periodic. Figure 11 shows burst-data (unaveraged) of near-surface (0.2 m) temperature, RABS, vertical velocity, the vertical velocity vertical gradient, turbulent kinetic energy, as well as corresponding conditional averages (i.e., averaged as a function of wave phase, right column). Phase was first identified by finding the depth maxima in the RABS contour whose average depth was closest to the DWL depth at this time (green dots in Figure 11b). The data were then divided into 80-s by 2-m windows centered on each peak and average across the windows. Temperature was windowed in time only, following the removal of a strong linear trend consistent with rapid cooling of the near-surface.

Periodic structures appear as asymmetric waves steepened/slanted in the downstream direction, with corresponding alternating regions of high and low RABS (Figure 11b). By downstream we mean in the direction the SWIFT is drifting, assuming it is with the surface flow (i.e., increasing in time). We briefly note that the strong periodicity in RABS further suggests they are not due to Langmuir cells (in addition to high La during this period, Figure 2c). We expect the drifters to become entrained in convergence zones, which should run directly orthogonal to overturning cells in the case of Langmuir turbulence. Contours are occasionally closed around high RABS regions, most notably at 340 s when the strongest RABS anomaly occurs. Conditionally averaged RABS emphasizes a clear pattern of expanded and collapsed contours on the upstream and downstream sides of the wave, respectively. Subtler corresponding patterns appear in temperature, velocity, vertical divergence (dw'/dz), and TKE, in part as a result of greater noise in these data. Conditionally averaged temperature suggests that high

RABS corresponds to a positive temperature anomaly within the layer and the lower RABS a negative anomaly (Figure 11a). This is consistent with warmer surface water being entrained downward while cooler water is moved up by the wave. Periodic, slanted alternating bands of upwelling and downwelling appear in vertical velocity, and the conditional average shows they run parallel to the steepened RABS contours (Figure 11c). However, the sign of vertical velocity seems to contradict the sense of upwelling and downwelling given by the RABS contours and temperature anomaly. In other words, the observed upwelling and downwelling appears about 180° out of phase with RABS and temperature. The bands in vertical velocity correspond to strong (vertical) divergence, also contradictory to the sense of convergence implied by the compressed RABS contours (Figure 11d). TKE within the layer is elevated with respect to below the layer and noisy, but exhibits a sharp interface at the base which follows wavy contours in RABS, indicating the TKE profile is strongly modulated by the periodic structures.

It is likely these periodic structures are high-frequency internal waves propagating along the DWL stratification. The asymmetry (steepening in the downwind direction) suggests that they are unstable, and a few closed contours may be the result of overturning and circulation around the anomaly entrained at depth. This would be consistent with the rapidly decreasing bulk Richardson number at this time, which suggests that the layer becomes unstable and may overturn in the afternoon (Figure 10). From these observations it seems likely that the unstable internal waves entrain the more turbulent surface water (i.e., with greater turbulent microstructure or bubbles generated at the surface, and thus higher RABS) to the base of the DWL. This vertical transport would occur on a time scale of about a minute, given vertical velocities up to 5 cm s^{-1} and a DWL depth of 2 m (Figure 11c).

The apparent contradiction between the sense of upwelling, downwelling and divergence given by the RABS contours and vertical velocity is puzzling. The patterns are otherwise in strong agreement, which suggests a sign error in the turbulent velocity data. However, we were unable to find such an error and the discrepancy remains unresolved. It is possible there is an unappreciated sign ambiguity in the EOF filtering method of Zeiden et al. (2023) which propagates to the resultant turbulent velocities. Alternatively, the discrepancy may arises from interpreting RABS as straightforward tracer. High TKE fluid, with a strong RABS signal, may be produced in the vicinity of strong fine-scale shear associated with the internal waves (Figure 11c). Acoustic field observations of unstable waves propagating along deep density layers show strong acoustic returns, presumably solely due to local TKE production as the background TKE is assumed to be low (e.g., Moum et al., 2003). In our observations, local TKE generation in the strong convergence region of the steepened downstream side of the internal wave could shift the positive RABS anomaly in the downstream direction.

6. Discussion

Each day DWLs were observed, dissipation rates were high relative to law-of-the-wall scaling within the layer and suppressed below (Figure 7). Estimates of the bulk Richardson numbers decrease each afternoon, suggesting the DWLs are likely unstable and susceptible to overturning (Figure 10). This interpretation is reinforced by close examination of RABS burst data with strongly periodic structures resembling high-frequency waves. Coincident patterns in temperature, RABS, vertical velocity, vertical divergence, and TKE are all characterized by strong along-flow asymmetry which suggests that the waves are unstable. However, while our observations suggest a correlation between the occurrence of elevated turbulent dissipation rates and the presence of structures in the DWL, we cannot constrain the internal mechanism elevating DWL turbulence levels. We lack observations to isolate terms in the turbulent kinetic energy momentum budget and establish which is dominant. Two mechanisms appear plausible: shear production and vertical transport.

Consistent with the literature, we observe strong shear associated with the DWL current (Figures 3 and 4). A reasonable hypothesis is that TKE production by enhanced DWL shear leads to elevated dissipation rates. Predictions for ϵ within the DWLs were improved by use of a shear-production scaling with an assumed linear decay profile for the turbulent stress (Figure 9). However, law-of-the-wall scaling provides a better average prediction across the full depth range of the observations (0.5–5 m). This suggests a more complex model which accounts for non-zero turbulent stress below the layer is required to improve predictions beyond the classic law-of-the-wall scaling. The true stress profile within the layer may also decay more slowly than linearly, which would lead to an under-prediction for ϵ within the layer. It is also important to note that the strongest shear was not often coincident with elevated DWL ϵ, and so the under-prediction by ϵ_S is perhaps not surprising. Additional shear production may occur on finer scales. While we do not observe turbulent shear, the regions of strong vertical convergence associated with the turbulent structures in the DWL suggests that fine-scale shear may be similarly strong.

Turbulent structures may also increase ϵ within the DWLs by transporting high TKE fluid from the surface to the base of the layer. Discussion in the literature has tended to focus on the role of shear instabilities as a source of turbulence, that is, when the perturbation (waves) traveling along the shear layer become unstable and "break." This may in part be because most observations have been in the deep ocean or at the base of the mixed layer, where background turbulence levels are expected to be very low. Controlled numerical and laboratory studies suggest that the breakdown of layer-scale coherent structures due to the onset of 3D turbulence occurs on the order of 100 times the shear time scale (Matsumoto & Hoshino, 2004). In our observations, this corresponds to a breakdown time scale of hours. In contrast, advective time scales associated with the periodic structures in this study are on the order of a minute. This suggests vertical transport of high TKE near-surface fluid may be the dominant homogenizing process on shorter time scales, while the breakdown of shear instabilities drives deepening over the course of a day.

7. Summary

In summary, we observed five strong DWL events under a range of forcing conditions, with temperature anomalies up to 3°C and velocity anomalies up to at least 0.1 m s^{-1}. Two patterns in wind stress were observed: (a) steady throughout the day and (b) calm mornings followed by an afternoon sea-breeze. The two strongest temperature anomalies (2 and 3°C) occurred on sea-breeze days when morning wind speeds were below 2 m s^{-1} and cloud coverage was minimal. Strong shear layers associated with velocity anomalies in the DWLs were present each day, often strongly concentrated at the base of the layer. We find burst-averaged TKE dissipation rates within all observed DWLs are on average higher than predicted by both log-layer scaling and shear-production scaling. Images of acoustic backscatter and TKE produced from the unaveraged data reveal turbulent structures during periods of elevated ϵ. Estimates of the bulk Richardson number imply that the DWL shear becomes unstable each afternoon. Close examination of a burst with strongly periodic structures within the DWL shows they resemble unstable high-frequency internal waves, consistent with this interpretation.

This study adds to a growing body of work showing the importance of resolving high-frequency, turbulent motions in DWLs to improve our understanding of the evolution of TKE therein. For example, a striking feature of the high-resolution images of TKE are strong gradients at the base of each layer, which are an order of magnitude greater than those suggested by the burst-averaged data (Figure 6). This discrepancy is due to time-averaging, which smears movement of the layer base due to turbulent structures in the layer. These observations are reminiscent of an early study using SWIFT drifters to measure dissipation rate in the upper 0.5 m, which showed elevated dissipation rates due to individual breaking waves (Thomson et al., 2016). A conclusion of that study was that choice of reference frame has a significant impact on the subsequent time-mean dissipation rate. A similar implication here is that the choice of averaging window will substantially affect the dissipation profile.

As in many previous DWL studies, the primary weakness of these observations is the limited number of realizations as we cannot compute meaningful statistics. Additionally, stratification and velocity data were measured on different platforms and so were neither collocated nor of comparable resolution. This leads to uncertainty in interpreting the observations when stratification and shear appeared to be misaligned, as on April 4. We have opportunistically leveraged relative acoustic backscatter data to identify turbulent structures, but the relationship between RABS and turbulence or fine-scale stratification is unknown. Future studies should be improved with sustained observations, for example, by mooring SWIFT drifters for a few months, as well as finer scale stratification data focused on the near surface from closely spaced thermistor chains suspended below SWIFTs.

Data Availability Statement

The SWIFT data used in this study can be downloaded from the following link, https://doi.org/10.5061/dryad.cvdncjt7s (Zeiden & Thomson, 2023). The codes used in data processing are publicly available at https://github.com/SASlabgroup/SWIFT-codes (Thomson & Zeiden, 2024).

Acknowledgments

We thank the crew and scientists of the R/V Sproul for deployment of the MLF and SWIFT drifters, as well as of the R/P FLIP and R/V Sally Ride for obtaining and making available the ancillary surface forcing data used in the study. We thank Alex de Klerk for instrument preparation and field data collection. We thank Dr. C. Bassett for work done to calibrate the acoustic backscatter data (Bassett & Zeiden, 2023). Funding was provided by the Office of Naval Research (Grant N00014-16-1-2545). Finally, we would also like to thank Dr. C. Luecke and Dr. K. Hughes for insightful discussions which influenced the analysis and feedback which improved the manuscript.

References

Banner, M. L., Babanin, A. V., & Young, I. R. (2000). Breaking probability for dominant waves on the sea surface. *Journal of Physical Oceanography*, *30*(12), 3145–3160. https://doi.org/10.1175/1520-0485(2000)030⟨3145:BPFDWO⟩2.0.CO;2

Bassett, C., Lavery, A., Ralston, D., Geyer, W., Jurisa, J., Thomson, J., et al. (2023). Acoustic backscattering at a tidal intrusion front. *Progress in Oceanography*, *219*, 103167. https://doi.org/10.1016/j.pocean.2023.103167

Bassett, C., & Zeiden, K. (2023). Calibration and processing of Nortek Signature1000 echosounders. APL-UW Tech Report 2307.

Belcher, S., Grant, A., Hanley, K., Fox-Kemper, B., Roekel, L. V., Sullivan, P., et al. (2012). A global perspective on Langmuir turbulence in the ocean surface boundary layer. *Geophysical Research Letters*, *39*(18), L18605. https://doi.org/10.1029/2012GL052932

D'Asaro, E., Farmer, D. M., Osse, J. T., & Dairiki, G. T. (1996). A Lagrangian float. *Journal of Atmospheric and Oceanic Technology*, *13*(6), 1230–1246. https://doi.org/10.1175/1520-0426(1996)013<1230:alf>2.0.co;2

Derakhti, M., Thomson, J., Bassett, C. S., Malila, M. P., & Kirby, J. T. (2023). Statistics of bubble plumes generated by breaking surface waves. Authorea. Inc. https://doi.org/10.22541/essoar.167751591.11265648/v1

Derakhti, M., Thomson, J., & Kirby, J. T. (2020). Sparse sampling of intermittent turbulence generated by breaking surface waves. *Journal of Physical Oceanography*, *50*(4), 867–885. https://doi.org/10.1175/JPO-D-19-0138.1

Fairall, C., Bradley, E., Hare, J., Grachev, A. A., & Edson, J. (2003). Bulk parameterization of air-sea fluxes: Updates and verification for the COARE algorithm. *Journal of Climate*, *16*(4), 571–591. https://doi.org/10.1175/1520-0442(2003)016<0571:bpoasf>2.0.co;2

Fairall, C., Bradley, E., Rogers, D., Edson, J., & Young, G. (1996). Bulk parameterization of air-sea fluxes for tropical ocean-global atmosphere coupled-ocean atmosphere response experiment. *Journal of Geophysical Research*, *101*(C2), 3747–3764. https://doi.org/10.1029/95JC03205

Farmer, D., & Armi, L. (1999). Stratified flow over topography: The role of small-scale entrainment and mixing in flow establishment. *Proceedings of the Royal Society of London. Series A*, *455*(455), 3221–3258. https://doi.org/10.1098/rspa.1999.0448

Fisher, A. W., & Nidzieko, N. J. (2024). AUV observations of Langmuir turbulence in a stratified shelf sea. *Journal of Physical Oceanography*, *54*(9), 1903–1920. https://doi.org/10.1175/JPO-D-23-0136.1

Francois, R. E., & Garrison, G. R. (1982). Sound absorption based on ocean measurements. Part II: Boric acid contribution and equation for total absorption. *Journal of the Acoustical Society of America*, *72*(6), 1879–1890. https://doi.org/10.1121/1.388673

Gargett, A. E. (1999). Velcro measurement of turbulence kinetic energy dissipation rate. *Journal of Atmospheric and Oceanic Technology*, *16*(12), 1973–1993. https://doi.org/10.1175/1520-0426(1999)016<1973:vmotke>2.0.co;2

Gartner, J. W. (2004). Estimating suspended solids concentrations from backscatter intensity measured by acoustic Doppler current profiler in San Francisco Bay, California. *Marine Geology*, *211*(3), 169–187. https://doi.org/10.1016/j.margeo.2004.07.001

Geyer, W., Lavery, A., Scully, M., & Trowbridge, J. (2010). Mixing by shear instability at high Reynolds number. *Geophysical Research Letters*, *37*(22), L22607. https://doi.org/10.1029/2010GL045272

Grare, L., Statom, N., Pizzo, N., & Lenain, L. (2018). Instrumented wave gliders for air-sea interaction and upper ocean research. *Frontiers in Marine Science*, *8*, 664728. https://doi.org/10.3389/fmars.2021.664728

Hughes, K., Moum, J., & Shroyer, E. (2020). Evolution of the velocity structure in the diurnal warm layer. *Journal of Physical Oceanography*, *50*(3), 615–631. https://doi.org/10.1175/JPO-D-19-0207.1

Hughes, K., Moum, J., Shroyer, E., & Smyth, W. (2021). Stratified shear instabilities in diurnal warm layers. *Journal of Physical Oceanography*, *51*, 2583–2598. https://doi.org/10.1175/JPO-D-20-0300.1

Hughes, K. G., Moum, J. N., & Shroyer, E. L. (2020). Heat transport through diurnal warm layers. *Journal of Physical Oceanography*, *50*(10), 2885–2905. https://doi.org/10.1175/JPO-D-20-0079.1

Kawaguchi, Y., Koenig, Z., Nomura, D., Hoppmann, M., Inoue, J., Fang, Y.-C., et al. (2022). Turbulent mixing during late summer in the ice–ocean boundary layer in the central arctic ocean: Results from the mosaic expedition. *Journal of Geophysical Research: Oceans*, *127*(8), e2021JC017975. https://doi.org/10.1029/2021JC017975

Lavery, A., Chu, D., & Moum, J. (2010). Measurements of acoustic scattering from zooplankton and oceanic microstructure using a broadband echosounder. *ICES Journal of Marine Science*, *67*(2), 379–394. https://doi.org/10.1093/icesjms/fsp242

Matsumoto, Y., & Hoshino, M. (2004). Onset of turbulence induced by a Kelvin-Helmholtz vortex. *Geophysical Research Letters*, *31*(2), L02807. https://doi.org/10.1029/2003GL018195

Moulin, A., Moum, J., & Shroyer, E. (2018). Evolution of turbulence in the diurnal warm layer. *Journal of Physical Oceanography*, *48*(2), 383–396. https://doi.org/10.1175/JPO-D-17-0170.1

Moum, J., Farmer, D., Smyth, W., Armi, L., & Vagle, S. (2003). Structure and generation of turbulence at interfaces strained by internal solitary waves propagating shoreward over the continental shelf. *Journal of Physical Oceanography*, *33*(10), 2093–2112. https://doi.org/10.1175/1520-0485(2003)033<2093:sagota>2.0.co;2

Perlin, A., Moum, J. N., Klymak, J. M., Levine, M. D., Boyd, T., & Kosro, P. M. (2005). A modified law-of-the-wall applied to oceanic bottom boundary layers. *Journal of Geophysical Research*, *110*(C10), C10S10. https://doi.org/10.1029/2004JC002310

Price, J., Mooers, C., & Leer, J. V. (1978). Observation and simulation of storm-induced mixed-layer deepening. *Journal of Physical Oceanography*, *8*(4), 582–599. https://doi.org/10.1175/1520-0485(1978)008⟨0582:OASOSI⟩2.0.CO;2

Price, J., Weller, R., & Pinkel, R. (1986). Diurnal cycling: Observations and models of the upper ocean response to diurnal heating, cooling and wind mixing. *Journal of Geophysical Research*, *91*(C7), 8411–8427. https://doi.org/10.1029/jc091ic07p08411

Richman, J. G., de Szoeke, R. A., & Davis, R. E. (1987). Measurements of near-surface shear in the ocean. *Journal of Geophysical Research*, *92*(C3), 2851–2858. https://doi.org/10.1029/JC092iC03p02851

Seim, H., Gregg, M., & Miyamoto, R. (1995). Acoustic backscatter from turbulent microstructure. *Journal of Atmospheric and Oceanic Technology*, *12*(2), 367–380. https://doi.org/10.1175/1520-0426(1995)0122.0.CO

Shcherbina, A. Y., D'Asaro, E. A., & Harcourt, R. R. (2019). Rain and sun create slippery layers in the eastern Pacific fresh pool. *Oceanography*, *32*(2), 98–107. https://doi.org/10.5670/oceanog.2019.217

Smyth, W. D., & Moum, J. N. (2000). Anisotropy of turbulence in stably stratified mixing layers. *Physics of Fluids*, *12*(6), 1343–1362. https://doi.org/10.1063/1.870386

Stokes, I. A., Kelly, S. M., Lucas, A. J., Waterhouse, A. F., Whalen, C. B., Klenz, T., et al. (2024). A generalized slab model. *Journal of Physical Oceanography*, *54*(3), 949–965. https://doi.org/10.1175/JPO-D-23-0167.1

Sutherland, G., Marie, L., Reverdin, G., Christensen, K., Brostrom, G., & Ward, B. (2016). Enhanced turbulence associated with the diurnal jet in the ocean surface boundary layer. *Journal of Physical Oceanography*, *46*(10), 3051–3067. https://doi.org/10.1175/jpo-d-15-0172.1

Thomson, J. (2012). Wave breaking dissipation observed with SWIFT drifters. *Journal of Atmospheric and Oceanic Technology*, *29*(12), 1866–1882. https://doi.org/10.1175/JTECH-D-12-00018.1

Thomson, J., Schwendeman, M. S., Zippel, S. F., Moghimi, S., Gemmrich, J., & Rogers, W. E. (2016). Wave-breaking turbulence in the ocean surface layer. *Journal of Physical Oceanography*, *46*(6), 1857–1870. https://doi.org/10.1175/JPO-D-15-0130.1

Thomson, J., & Zeiden, K. (2024). SWIFT-codes. https://doi.org/10.5281/zenodo.13922183

Thorpe, S. A. (1978). The near-surface ocean mixing layer in stable heating conditions. *Journal of Geophysical Research*, *83*(C6), 2875–2885. https://doi.org/10.1029/JC083iC06p02875

Vagle, S., Gemmrich, J., & Czerski, H. (2012). Effect of upper ocean stratification on turbulence and optically active bubbles. *Journal of Geophysical Research*, *117*(C00H16), C00H16. https://doi.org/10.1029/2011JC007308

Wijesekera, H., Wang, D., & Jarosz, E. (2020). Dynamics of the diurnal warm layer: Surface jet, high-frequency internal waves and mixing. *Journal of Physical Oceanography*, *50*(7), 2053–2070. https://doi.org/10.1175/JPO-D-19-0285.1

Wiles, P., Rippeth, T. P., Simpson, J., & Hendricks, P. (2006). A novel technique for measuring the rate of turbulent dissipation in the marine environment. *Geophysical Research Letters*, *33*(21), L21608. https://doi.org/10.1029/2006gl027050

Zeiden, K., & Thomson, J. (2023). ADCP data collected in the southern California Bight by SWIFT drifters as part of the ONR "Langmuir Circulation Departmental Research Initiative (LC-DRI)" [Dataset]. *Dryad*. https://doi.org/10.5061/dryad.cvdncjt7s

Zeiden, K., Thomson, J., & Girton, J. (2023). Estimating profiles of dissipation rate in the upper ocean from acoustic Doppler measurements below surface following platforms. *Journal of Atmospheric and Oceanic Technology*.

Zippel, S. F., Farrar, J. T., Zappa, C. J., & Plueddemann, A. J. (2022). Parsing the kinetic energy budget of the ocean surface mixed layer. *Geophysical Research Letters*, *49*(2), e2021GL095920. https://doi.org/10.1029/2021GL095920